THE SCALING OF THE ION HEATING AND ELECTROSTATIC POTENTIAL IN SPHERICAL TOKAMAK

T. Ahmadi, Y. Ono, H. Tanaka and H. Tanabe Graduate school of frontier sciences, University of Tokyo Tokyo, Japan

Email: tara.ahmadi.smart@gmail.com

Abstract

We report direct evidence that reconnection–driven electrostatic potentials control downstream ion heating in TS-6 merging plasmas. Synchronized soft X-ray, multi-tip Langmuir, and Thomson scattering measurements resolve a quadrupolar plasma potential whose gradient defines a localized reconnection field, $E_p \simeq \nabla \Phi_p$, that is 4–6× larger than the inductive field $E_{\rm ind}$. The potential amplitude obeys an empirical scaling $\Delta \Phi \propto B_{\rm rec} B_g$, and the downstream ion-temperature rise follows $\Delta T_i \propto B_{\rm rec}^2$ at fixed $B_g/B_{\rm rec}$, consistent with pickup/acceleration across the potential lobe. Particle-in-cell simulations (reduced mass ratio) reproduce the spatial structure and field magnitudes within $\sim 20\%$ and recover the observed ordering $E_p \gg E_{\rm ind}$. Cross-correlation in time shows the causal sequence SXR burst $\to \Delta \Phi$ growth $\to \Delta T_i$ increase, while a species trend consistent with ρ_i/ℓ_E further supports the mechanism. These results identify a controllable electrostatic route to ion heating and provide actionable guidance for choosing $B_g/B_{\rm rec}$ to optimize exhaust heating in reactor-relevant reconnection regimes.

1. INTRODUCTION

Magnetic reconnection—the rapid rearrangement of magnetic field lines—is a universal process in astrophysical and laboratory plasmas [1, 2, 3], converting magnetic energy into particle acceleration and plasma heating. It underlies phenomena from solar flares to tokamak sawtooth collapses[4]. A central question is how energy is partitioned between ions and electrons, particularly in strong guide-field configurations.

In spherical tokamaks (STs), merging plasma rings drive reconnection, enabling plasma startup and bulk ion heating up to keV scales, as seen in TS-3[5], TS-4[6], MAST[7], ST-40[8], and TS-6[9]. Empirically, ion heating scales with the square of the reconnecting magnetic field, $\Delta T_i \propto B_{Rec}^2$ [10], though its underlying mechanism has remained partially understood.

High guide-field reconnection produces strong field-aligned electric fields that accelerate electrons at the X-point and downstream, forming high-energy tails and x-ray bursts. These electrons induce charge separation, generating a quadrupolar floating potential structure predicted in simulations and inferred in MRX and MAST[11, 12]. This potential creates an in-plane electric field, E_p , often several times stronger than the inductive field, driving ions via $E_p \times B_g$ drift, with directed outflow energy thermalized downstream[13]. Despite this framework, direct experimental validation of the potential structure and its link to ion heating has been scarce.

This study combines high-resolution diagnostics, modeling, and simulations in TS-6. A 2D Langmuir probe array reveals a quadrupolar floating potential exceeding 200 [V] with asymmetry across high- and low-field sides. Ion Doppler tomography maps show localized downstream heating correlated with the potential growth, while soft x-ray imaging [14] captures electron bursts synchronized with the potential gap. Together, these results trace a consistent chain: electron acceleration \rightarrow charge separation \rightarrow floating potential \rightarrow in-plane electric field \rightarrow ion heating.

Theoretical analysis, based on electron force balance and high guide-field reconnection geometry, predicts the potential gap $\Delta\Phi$ and in-plane field $E_p\sim \Delta\Phi/l_\perp$, driving ion outflows $v_{E\times B}\propto B_{Rec}$ and yielding $\Delta T_i\propto B_{Rec}^2$, consistent with observations. Two-fluid Hall-MHD and particle-in-cell simulations reproduce the potential structure[15], its dependence on B_{Rec} and B_g , and species-specific ion pickup, including reduced heating at very large guide fields and enhanced heating for heavier ions.

These findings have practical relevance for reactor-scale STs. Merging startup offers a robust, non-inductive route to high- β plasmas, but efficiency depends on maximizing ion heating. Optimizing the balance between reconnecting and guide fields is essential: too low a guide field reduces stability, while too high suppresses ion heating. Ion species and impurities must also be considered. By providing a unified experimental and theoretical explanation for the B_{Rec}^2 scaling and guide-field effects, this work establishes a predictive basis for optimizing reconnection startup in current and future ST devices.

2. EXPERIMENTAL SETUP

The experiments were carried out on the TS-6 spherical tokamak[9, 16] at the University of Tokyo, which is designed to study plasma startup by flux-rope merging under high guide-field conditions. The vacuum vessel is cylindrical with a radius of 0.375 m and a length of 1.44[m], equipped with a set of internal poloidal field (PF) coils, a central toroidal field solenoid, a separation (SP) coil, and equilibrium field (EF) coils. Two 4-turn PF coils are used to inductively generate initial plasma rings, while the 3-turn SP coil controls the inward motion of the rings toward the mid-plane. The toroidal field is provided by the central solenoid (up to $I_{TF} \sim 50$ [kA-turn]), and the EF coils (234 turns each, with $I_{EF} \sim 0.15$ [kA] in DC operation) establish vertical equilibrium fields. Figure 1(a) illustrates the device configuration, while Figure 1(c) shows a sequence of high-speed camera images capturing the plasma formation, merging, and equilibrium phases.

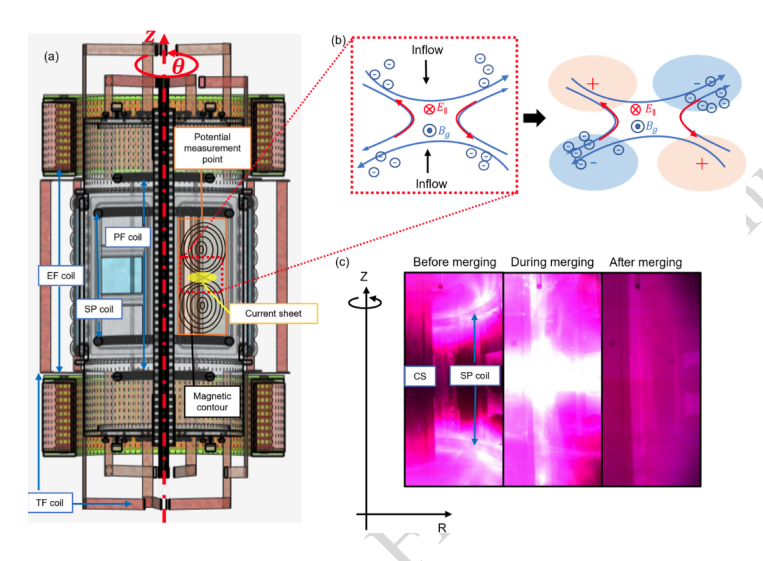


FIG. 1. (a) Schematic view of the TS-6 Tokamak merging device. Solid black lines indicate magnetic flux contours, while potential measurements are conducted in the global area (orange region). (b) Schematic diagrams of the charge separation process in the X-point region during the merging reconnection process. (c) High-speed camera image showing the plasma formation, merging, and equilibrium stages.

During each discharge, two plasma rings form inductively around the PF coils at the top and bottom of the vessel. As the PF coil currents decay to zero, the rings detach and move toward the mid-plane under the mutual attraction of parallel plasma currents. The SP coil current enhances this inward motion, leading to collision and reconnection on a timescale of \leq 0.1 [ms]. After reconnection, the plasma rapidly thermalizes into a single high-temperature core at the mid-plane, where temperatures are several times higher than the initial values.

A comprehensive set of diagnostics was deployed to characterize magnetic, electrostatic, and kinetic properties during the merging process: (a) Magnetic probe array: A two-dimensional array of pickup coils with radial resolution $\Delta Z \sim 1.1$ [cm] is installed across $-0.23 \text{m} \leq Z \leq 0.25 \text{[m]}$ and $0.075 \text{[m]} \leq R \leq 0.335 \text{[m]}$. The array measures all three components of the magnetic field, allowing reconstruction of poloidal flux surfaces and evaluation of the reconnecting electric field via Faraday's law, $E_{Rec} = -\partial A_{\phi}/\partial t$; (b) Ion Doppler tomography: Local ion temperature was measured with a high-resolution Doppler tomography system consisting of 288 viewing chords (16 radial \times 18 axial). Collected spectra were dispersed by a Czerny–Turner spectrometer (focal length 1000 [mm], grating 1800 [L/mm], NA=0.06). The system provides two-dimensional $T_i(R,Z)$ maps with coverage across $0.076 \text{m} \leq R \leq 0.27 \text{m}$. Because the ion–neutral relaxation time is short ($\sim 0.7 \mu \text{s}$), the neutral particle temperature was taken as a proxy for local ion temperature; (c) Floating potential measurements: A Langmuir probe array mounted on the R-Z plane ($-0.15 \text{m} \leq Z \leq 0.15 \text{m}$ and $-0.1 \text{m} \leq R \leq 0.32 \text{m}$) was used to measure the floating potential Φ_f , enabling the calculation of Φ_p . The plasma potential was inferred from

$$\Phi_f = \Phi_p + \frac{\kappa T_e}{e} \left(\frac{Zn_i}{n_e} - \frac{1}{2} \right) \tag{1}$$

where T_e was obtained from probe I–V characteristics near the X-point; and (d) Soft x-ray diagnostics: A tangential soft x-ray (SXR) fast imaging system was used to detect bursts of energetic electrons associated with the reconnection electric field near the X-point. This diagnostic was particularly important for correlating the timing of electron acceleration with the onset of the floating potential structure[17].

Together, these diagnostics enable simultaneous measurement of magnetic reconnection dynamics, potential structures, ion heating, and electron acceleration. This comprehensive coverage allows us to test the hypothesis that electron-driven charge separation produces a quadrupolar potential, generating an in-plane electric field that accelerates and heats ions during the merging process.

3. EXPERIMENTAL RESULTS

After breakdown, two plasma rings form around the PF coils, which decay on a $\sim 100\,\mu s$ timescale. As I_{PF} decreases, the rings detach and move toward the mid-plane, driven by mutual attraction and the SP coil field.

Magnetic reconnection begins at $T\approx 465\,\mu\mathrm{s}$, identified by changes in flux surfaces, a rise in reconnection electric field, and downstream ion heating. The process is rapid (< 0.1 ms), comparable to the Alfvén time of TS-6, and consistently produces a single merged plasma core. This reproducibility enables controlled studies of how B_{Rec} and B_q affect potential structures and ion heating, with diagnostics synchronized to this sequence.

3.1. Two-dimensional ion temperature and floating potential profiles

Figure 2(a) show ion heating structures. Before reconnection, T_i is uniform (10–20 eV). At onset, a hot spot rapidly forms downstream on the HFS, where T_i rises by a factor of 3–5. Tomography (288 sightlines, $\sim 1-2$ [cm] resolution) shows heating localized where reconnection outflows stagnate, consistent with flow-to-thermal energy conversion.

Simultaneously, Langmuir probes detect a quadrupolar Φ_f exceeding 200 V, far above background fluctuations. Its growth precedes or overlaps with ion heating, with stronger HFS potentials reflecting asymmetric B_g . These data suggest the sequence: electron acceleration \rightarrow quadrupolar $\Phi_f \rightarrow E \times B$ ion acceleration \rightarrow thermalization, forming the experimental basis for electrostatic-field-driven ion heating in TS-6.

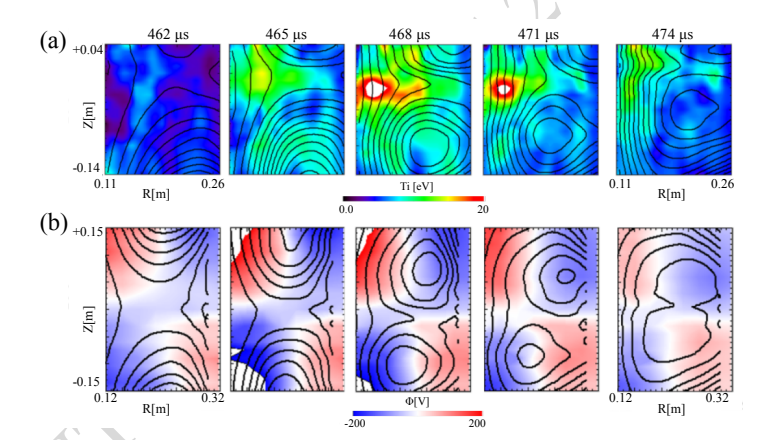


FIG. 2. (a) Time evolution of the 2D ion temperature profile measured by 2D ion Doppler. (b) Electrostatic potential along with the magnetic flux lines.

Figure 2(b) shows the quadrupolar $\Phi_f(R,Z)$ pattern, extending from the X-point along the separatrix. It reflects charge separation from electron acceleration along B_g , balanced by an electrostatic potential. A midplane cut shows the steepest gradients near Z=0. The potential gap $\Delta\Phi=\max(\Phi_f)-\min(\Phi_f)$ reaches 200–250 V, implying in-plane fields $E_p\sim 2\times 10^3$ V/m, far exceeding E_{Rec} .

The HFS amplitude is ~ 100 V larger than the LFS, consistent with stronger B_g and explaining the localization of ion heating. These results provide direct experimental evidence that the quadrupole potential governs ion dynamics.

3.2. Scaling of potential gap and ion heating with reconnecting and guiding fields

Figure 3 summarizes the B_{Rec} dependence. Panel (a): $\Delta\Phi\propto B_{Rec}$, showing that stronger reconnecting fields drive larger potentials via enhanced electron acceleration. Panel (b): ion heating follows $\Delta T_i\propto B_{Rec}^2$, consistent with $E_p\times B_g$ drift scaling ($m_iv^2\propto B_{Rec}^2$). Figure 3 has a baseline floating-potential offset which could be due to the Te-dependent conversion, probe bias, or limited B_{rec} dynamic range during the experimental measurements. Spatial T_i profiles confirm that higher B_{Rec} increases both maximum ΔT_i and heated area, while retaining HFS localization. Thus, TS-6 establishes a consistent experimental link: $B_{Rec}\to\Delta\Phi\propto B_{Rec}\to\Delta T_i\propto B_{Rec}^2$, providing a framework for reconnection-driven startup in spherical tokamaks.

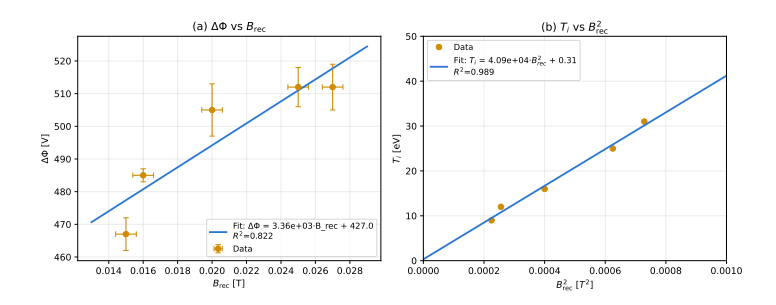


FIG. 3. (a) Potential gap, $\Delta\Phi$, formed during the merging process under a constant guide field ($B_g \sim 0.16T$) as a function of the reconnecting magnetic field, $B_{\rm rec}^2$. (b) Ion temperature increase as a function of the reconnecting magnetic field.

The effect of the guide field on potential structure and ion heating is shown in Fig. 4. With B_{Rec} fixed, the potential gap $\Delta\Phi$ grows linearly with B_g [Fig. 4(a)], consistent with the picture that stronger B_g aligns with the parallel inductive field, enhancing electron acceleration, charge separation, and polarization. The observed $\Delta\Phi\propto B_g$ scaling is therefore a direct signature of electron-driven polarization in high guide-field reconnection.

Ion heating [Fig. 4(b)] shows a different trend: ΔT_i rises at moderate B_g but saturates and eventually decreases as B_g/B_{Rec} becomes large. This suppression reflects competing roles of B_g : while it enhances electron acceleration and potential strength, a very strong guide field reduces the efficiency of $E_p \times B_g$ ion heating.

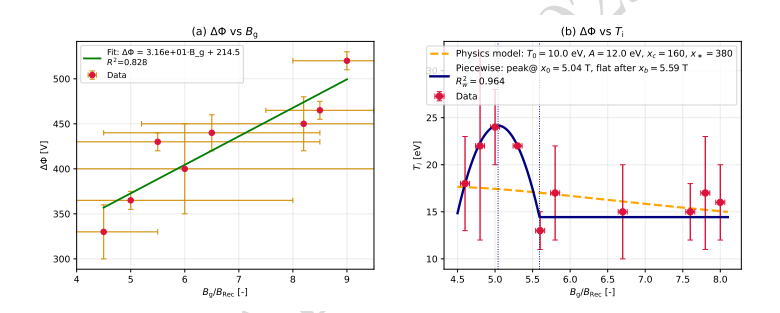


FIG. 4. (a) Potential gap, $\Delta\Phi$, and (b) ion temperature, T_i , as functions of the guide field ratio $B_g/B_{\rm rec}$ under a constant reconnecting magnetic field ($B_{\rm rec} \sim 0.018T$). The green and blue line showing the fitting related to the measurement data

3.3. Correlation with energetic electrons and SXR emission

SXR diagnostics reveal the temporal chain linking electrons, potentials, and ions. A sharp SXR burst at $T=467~\mu s$ marks electron acceleration near the X-point [Fig. 5(a)–(b)]. Immediately after, the quadrupolar floating potential develops [Fig. 5(c)], followed by downstream ion heating. The sequence — electron acceleration $\to \Delta \Phi$ formation $\to E_p$ field \to ion heating — directly demonstrates the causal pathway for energy conversion. SXR data also clarify energy partition: the electron burst is localized, but the resulting potential is global, coupling electron energy to bulk ions via $E_p \times B_g$. Thus, electrons act as the catalyst: accelerated first, they generate $\Delta \Phi$, which then drives ion heating on macroscopic scales. These synchronized measurements provide one of the clearest experimental validations of guide-field reconnection theory and simulations.

3.4. Species dependence: hydrogen versus argon

To probe ion-mass effects, experiments were repeated with argon. Under similar fields ($B_{Rec} \sim 0.03$ T, $B_g \sim 0.15$ T, $n_e \sim 5 \times 10^{20}$ m⁻³), downstream T_i reached ~ 80 eV, much higher than in hydrogen. The difference arose despite similar $\Delta\Phi$ and reconnection timescales, pointing to distinct ion responses.

The key lies in ρ_i/l_E . For hydrogen $(T_i \sim 10 \text{ eV})$, $\rho_i \sim 2\text{--}3 \text{ mm} \ll l_E \sim 1 \text{ cm}$, so ions remain magnetized and gain energy smoothly via $E_p \times B_g$. For argon, $\rho_i \sim 15 \text{ mm} \geq l_E$, placing ions in a ballistic pickup regime: accelerated directly by the local E, they acquire large directed energy in a single gyro-orbit, which thermalizes downstream. Tomography confirms heating localized near the separatrix, broadening downstream as flows stagnate [18, 19, 11].

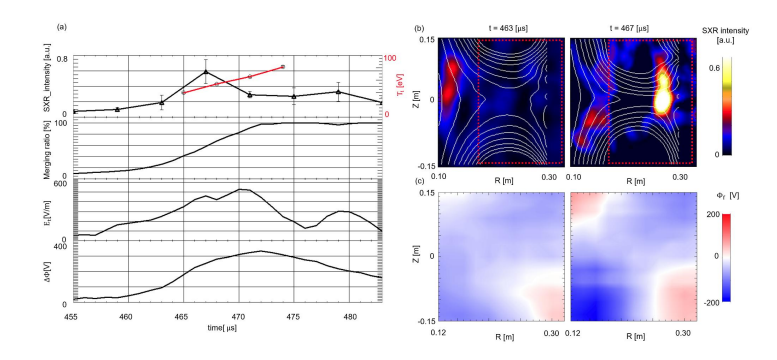


FIG. 5. (a) From top to bottom: (left axis) time evolution of soft X-ray (SXR) emission intensity around the X-point, corresponding to the red dotted square in (b); (right axis) ion temperature T_i , merging ratio, toroidal electric field E_t , and potential gap $\Delta\Phi$. (b) 2D profile of the SXR emission image. Magnetic flux lines are shown in white. (c) 2D contour of the floating potential, Φ_f , corresponding to the SXR measurement region.

These results highlight that only ions with sufficiently large ρ_i/l_E ratios exhibit enhanced heating, in agreement with theory. They also imply practical consequences for reactor startups: heavier fuel or impurity ions (D, T, Ar, Ne, Kr) can locally enhance conversion, but excessive content may cause nonuniform heating and radiative loss. Controlling this balance will be critical for high- β spherical tokamaks.

4. PARTICLE-IN-CELL (PIC) SIMULATION SETUP

To interpret and extend the experimental observations, we performed fully kinetic simulations using the VPIC code [20, 21]. The purpose of these simulations is to capture the role of charge separation and quadrupolar potential formation in driving ion heating during spherical tokamak (ST) merging.

The reconnecting magnetic configuration was initialized using a two-plasmoid coalescence model, expressed through the out-of-plane vector potential

$$A_y(x,z) = B_0 \lambda \ln \left[\cosh \left(\frac{z}{\lambda} \right) + 0.4 \cos \left(\frac{x}{\lambda} \right) \right], \tag{2}$$

where B_0 is the initial reconnecting field amplitude and λ is the equilibrium current sheet half-thickness. This choice generates two merging flux ropes with a localized X-point at the mid-plane. A uniform guide field B_g is imposed along the y direction and held constant throughout each run.

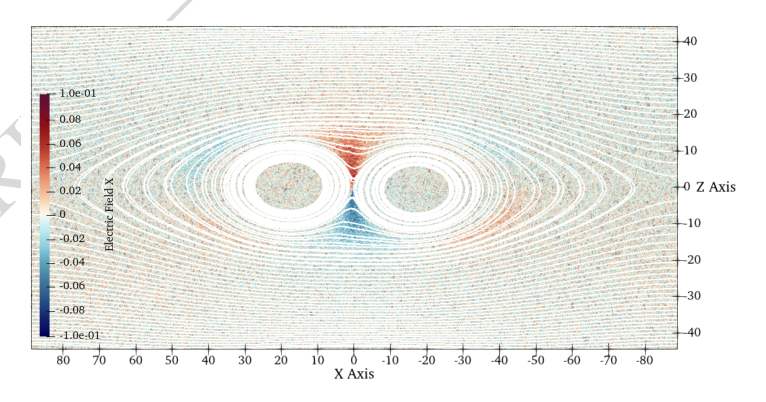


FIG. 6. The 2D render of ion outflow velocity in VPiC simulation corresponding to the experimental setup along with the flux contours

The computational box spans

$$x \in [-2\pi\lambda, 2\pi\lambda], \quad y \in [-0.5\pi\lambda, 0.5\pi\lambda], \quad z \in [-\pi\lambda, \pi\lambda],$$

sufficient to encompass both current layers and the downstream exhausts. Boundary conditions are chosen to minimize artificial reflections: the x direction is periodic (representing the reconnecting direction), while y and z use perfectly conducting, particle-reflecting boundaries.

The initial ion and electron temperatures are equal $(T_{i0}=T_{e0})$, ensuring comparable thermal pressures at t=0. The ion-to-electron mass ratio is reduced to $m_i/m_e=200$ to make the computation tractable, while maintaining adequate scale separation. The ratio of electron plasma to cyclotron frequency is set to $\omega_{pe}/\Omega_{ce}=2$, placing the system in the high-guide-field kinetic regime relevant to the TS-6 merging experiments. The initial current is carried self-consistently by drifting ions and electrons, with drift velocities chosen such that $J_y=en_0(v_{iy}-v_{ey})$ satisfies Ampère's law for the equilibrium fields.

The simulations resolve both the Debye length and electron skin depth with $\Delta x 0.3 \lambda_D$ and $\Delta t 0.3 / \omega_{pe}$. Typically, 200 particles per cell per species are employed, which is sufficient to suppress numerical noise in the electrostatic potential. Runs are evolved up to $t \sim 50 \, \Omega_{ci}^{-1}$, by which time reconnection has saturated and both quadrupolar potential structures and ion outflows are well developed.

5. PIC SIMULATION RESULTS

The kinetic simulations reproduce the main experimental signatures of merging reconnection: the formation of a quadrupolar floating potential, the scaling of the potential gap with both reconnecting and guide fields, and the dominance of electrostatic fields over inductive fields in driving ion heating.

Figure 7 shows the electrostatic potential $\Phi(x,z)$ extracted at peak reconnection from the VPIC runs. A clear four-lobe (quadrupolar) structure develops around the X-point, with the positive and negative lobes aligned along the separatrices. This pattern matches directly the Langmuir probe maps in TS-6 (cf. Fig. 7), validating that the observed probe signals arise from self-consistent charge separation in the kinetic layer. The simulated $\Delta\Phi$ values, measured as the difference between the positive and negative lobes, are within 20% of the experimental values, the simulations tending to overpredict due to periodic-x/reflecting-(y,z) and mi/me=200 can over-stiffen structures.

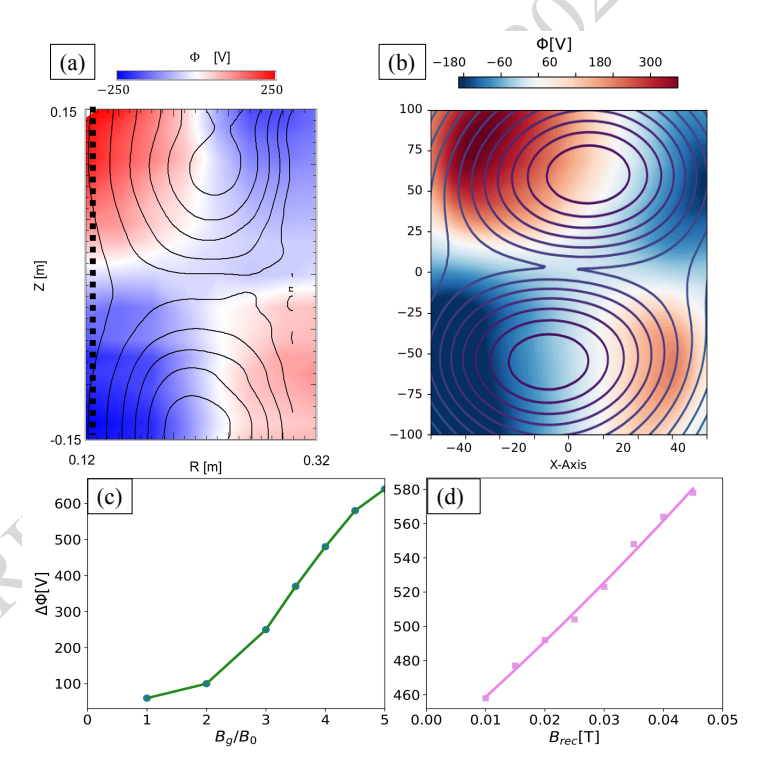


FIG. 7. a) TS-6 experiment: Electrostatic potential profile along with poloidal flux contours. (b) 3D kinetic simulation of plasma merging: Electrostatic potential profile with poloidal flux contours. (c) Dependence of the potential gap on the guide field. (d) Dependence of the potential gap on the reconnecting magnetic field.

Across a scan of reconnecting and guide fields, the potential gap in PIC runs is well fit by

$$\Delta\Phi \simeq C_{\rm PIC} B_{\rm rec} B_q, \tag{3}$$

with $C_{\rm PIC} \approx 3.2 \times 10^3$ (SI units), consistent with the fit to experimental data. This linear scaling in both $B_{\rm rec}$ and B_g is the same functional form predicted by the analytic theory, where

$$\Delta\Phi_{\rm th} = \frac{\epsilon L}{\sqrt{\mu_0 m_i n}} B_{\rm rec} B_g. \tag{4}$$

Equation (4) shows that the coefficient $C_{\rm eff}$ should vary as $1/\sqrt{n}$ in addition to geometric factors. In the present PIC scans, n is held fixed, so the theoretical $1/\sqrt{n}$ dependence is absorbed into a constant $C_{\rm eff}$. Using $\epsilon \sim 0.05$, $L \sim 5$ cm, and $n \sim 3 \times 10^{20} \, {\rm m}^{-3}$, the theoretical coefficient evaluates to $C_{\rm eff} \approx 3.1 \times 10^3$, in close agreement with the fitted $C_{\rm PIC}$. This confirms that the PIC scaling is quantitatively consistent with the analytic model and experiment.

From the simulated potential maps we calculate the in-plane electrostatic field

$$E_{p,\text{max}} \simeq \frac{\Delta \Phi}{\ell_{\perp}},$$
 (5)

with ℓ_{\perp} defined as the FWHM width of the potential lobes ($\ell_{\perp} \approx 0.1$ m, consistent with TS-6). Typical values reach $E_{p,\mathrm{max}} \sim 2 \times 10^3 \, \mathrm{V/m}$, which is four to six times larger than the inductive reconnection field $E_{\mathrm{rec}} \sim 300-500 \, \mathrm{V/m}$ inferred from $\dot{\psi}$. Thus, as in the experiment, the dominant field experienced by ions in the PIC runs is electrostatic.

Although $\Delta\Phi$ grows linearly with B_g , the ratio

$$\frac{E_{p,\text{max}}}{B_q} \simeq \frac{\Delta \Phi}{\ell_{\perp} B_q} \propto B_{\text{rec}},\tag{6}$$

is independent of B_g for fixed $B_{\rm rec}$. This produces a plateau when plotted versus $B_g/B_{\rm rec}$ (Fig. 7), consistent with the "kinematic ceiling". PIC runs show only weak scatter about this plateau, confirming that the saturation of ion heating at large guide fields is due to the cancellation of B_g in E_p/B_g .

Ion heating in PIC is quantified by the increment

$$\Delta T_i = \frac{m_i}{2} \left(\langle v^2 \rangle - \langle v^2 \rangle_{t=0} \right),$$

evaluated in downstream regions. As in TS-6, ΔT_i scales quadratically with the reconnecting field, $\Delta T_i \propto B_{\rm rec}^2$, in agreement with the analytic scaling derived from $v_{E\times B}^2$. At fixed $B_{\rm rec}$, $\Delta T_i(B_g)$ exhibits a rise-plateau-decline behavior: increasing at small B_g , flattening once E_p/B_g saturates, and declining when large guide fields reduce viscous and compressional dissipation efficiency. This trend mirrors the guide-field suppression curve observed experimentally, reinforcing the interpretation that the efficiency factor $\alpha(B_g)$ governs the downturn at large B_g .

6. SUMMARY.

Taken together, the VPIC simulations demonstrate that the essential experimental observations can be reproduced and understood as robust kinetic effects. First, the formation of a quadrupolar electrostatic potential is a generic outcome of collisionless reconnection: it arises from charge separation along the separatrices and is directly visible in the potential maps. This quadrupolar pattern is nearly identical to the floating potential structures measured by Langmuir probes in TS-6, confirming that the diagnostic signals are physical rather than instrumental. The magnitude of the simulated potential gaps is within 20% of experiment, with the overprediction plausibly attributable to the reduced mass ratio and idealized boundary conditions. This level of agreement gives confidence that the code is resolving the dominant processes.

Second, the scaling of the potential gap with $B_{\rm rec}$ and B_g is fully consistent between PIC, experiment, and theory. The PIC results collapse onto the simple empirical form $\Delta\Phi=C_{\rm PIC}\,B_{\rm rec}B_g$, with $C_{\rm PIC}\approx 3.2\times 10^3$, while the analytic theory predicts $\Delta\Phi=(\epsilon L/\sqrt{\mu_0m_in})\,B_{\rm rec}B_g$. For the density and geometry relevant to TS-6, the theoretical prefactor evaluates to 3.1×10^3 , essentially indistinguishable from the simulation fit. This agreement is not trivial: it confirms that the product scaling arises from first principles, and that the PIC runs, despite reduced m_i/m_e , capture the correct electron force balance responsible for establishing Φ .

Third, the decomposition of fields shows that the in-plane electrostatic field is dominant over the inductive reconnection field. This hierarchy is critical because it establishes the pathway of energy transfer: ions are not heated primarily by inductive acceleration at the X-point, but by E_p associated with Φ gradients, which subsequently drive flows that thermalize downstream. The PIC quantification of E_{ind} (4–6 smaller than E_p) corroborates the experimental finding that probe-inferred E_p substantially exceeds the inductive field inferred from magnetic flux variation.

Fourth, the guide-field dependence is captured naturally. While $\Delta\Phi$ continues to grow linearly with B_g , the normalized quantity $E_{p,\max}/B_g$ saturates, producing a plateau independent of B_g . This "kinematic ceiling" agrees with analytic predictions and provides the mechanism for the observed saturation of ion heating. In addition, the runs show that as B_g becomes large, the efficiency of converting bulk flow into heat decreases, consistent with reduced cross-field viscosity and diminished ballistic pickup when ρ_i becomes small compared to the E_p gradient scale. The result is a rise-plateau-decline trend in $\Delta T_i(B_g)$, matching the experimental suppression curves.

Finally, the ion heating scalings are faithfully reproduced. For varying $B_{\rm rec}$ at fixed B_g , PIC yields $\Delta T_i \propto B_{\rm rec}^2$, which follows directly from the quadratic dependence on $v_{E\times B}$ in the downstream control volume. For varying B_g at fixed $B_{\rm rec}$, the rise-plateau-decline form emerges naturally, illustrating that guide-field suppression is not an artifact of collisional physics but a kinetic inevitability once E_p/B_g saturates and dissipation efficiency $\alpha(B_g)$ falls. These trends not only align with the probe-inferred heating but also with the theoretical framework.

In summary, the VPIC results provide a fully kinetic validation of the experimental scalings and the analytic model. The agreement across three independent approaches — laboratory data, theory, and particle-in-cell simulation — demonstrates that the scaling $\Delta\Phi\propto B_{\rm rec}B_g$ with an effective prefactor $C_{\rm eff}\sim 3\times 10^3$, the dominance of E_p over $E_{\rm ind}$, the kinematic ceiling in E_p/B_g , and the resulting behavior of ΔT_i are all universal features of guide-field reconnection in the TS-6 regime. This convergence strongly supports the conclusion that reconnection-driven startup heating in spherical tokamaks can be explained as an interplay of electrostatic potential formation and guide-field-modulated thermalization efficiency, processes that are robust to the idealizations in the simulation and directly relevant to reactor-scale extrapolation.

REFERENCES

- [1] J. L. Burch and T. D. Phan. In: Geophys. Res. Lett. 43 (2016), p. 16.
- [2] M. Gobbin et al. In: Nucl. Fusion 62 (2022), p. 026030.
- [3] T. Gou et al. In: *ApJL* 845 (2017), p. L1.
- [4] Y. B. Nam et al. In: *Nucl. Fusion* 58 (2018), p. 066009.
- [5] Y. Ono et al. In: Phys. Rev. Lett. 76 (1996), p. 3328.
- [6] E. Kawamori and et al. In: Nucl. Fusion 47 (2007), pp. 1232–1237.
- [7] A. Sykes and et al. In: Nucl. Fusion 41 (2001), p. 1423.
- [8] M. Gryaznevich et al. In: Nucl. Fusion 62 (2022), p. 4.
- [9] H. Tanabe and et al. In: Plasma Fusion Research 8 (2013), p. 2405088.
- [10] T. Ahmadi and Y. Ono. In: Nucl. Fusion 61 (2021), p. 126007.
- [11] J. Yoo et al. In: *Physics of Plasmas* 21 (2014), p. 055706.
- [12] H. Tanabe et al. In: Phys. Rev. Lett. 115 (2015), p. 215004.
- [13] Y. Ono et al. In: Phys. Rev. Lett. 107 (2011), p. 185001.
- [14] J. Xiang et al. In: Rev. Sci. Instrum. 92 (2021), p. 083504.
- [15] K. Yamazaki et al. In: *Physics of Plasmas* 22 (2015), p. 101202.
- [16] Y. Ono et al. In: *Physics of Plasmas* 22 (2015), p. 055708.
- [17] H. Tanabe et al. In: *Nucl. Fusion* 59 (2019), p. 8.
- [18] J. Birn and et al. In: Space Sci. Rev. 173 (2012), p. 49.
- [19] J. F. Drake et al. In: J. Geophys. Res. 114 (2009), A05111.
- [20] A. Stanier et al. "The role of guide field in magnetic reconnection driven by island coalescence". In: *Phys. Plasmas* 24.2 (2017), p. 022124. DOI: 10.1063/1.4976712.
- [21] J. Ng et al. In: ArXiv. https://doi.org/10.1063/1.4935302 1 (2015), p. 4935302.